AGU ADVANCING EARTH AND SPACE SCIENCES

Geophysical Research Letters

RESEARCH LETTER
10.1029/2024GL108233

When, Where and to What Extent Do Temperature Perturbations Near Tropical Deep Convection Follow Convective Quasi Equilibrium?

Yi-Xian Li[1,2], Hirohiko Masunaga[2], Hanii Takahashi[3], and Jia-Yuh Yu[1]

[1]Department of Atmospheric Sciences, National Central University, Taoyuan, Taiwan, [2]Institute for Space-Earth Environmental Research, Nagoya University, Nagoya, Japan, [3]Jet Propulsion Laboratory, California Institute of Technology, Pasadena, CA, USA

Key Points:

- Tropical temperature perturbations near extreme deep convection rapidly conform to convective quasi equilibrium in a three-hour window
- Only the top 7% precipitating deep convection can modulate hourly tropical temperature patterns beyond a 1° radius
- Top 1% precipitating deep convection constrains nearby temperature perturbations up to an 9° radius during peak precipitation

Supporting Information:

Supporting Information may be found in the online version of this article.

Correspondence to:

Y.-X. Li and J.-Y. Yu,
Yi-Xian.Li@monash.edu;
jiayuh@atm.ncu.edu.tw

Citation:

Li, Y.-X., Masunaga, H., Takahashi, H., & Yu, J.-Y. (2024). When, where and to what extent do temperature perturbations near tropical deep convection follow convective quasi equilibrium? *Geophysical Research Letters*, *51*, e2024GL108233. https://doi.org/10.1029/2024GL108233

Received 8 JAN 2024
Accepted 13 MAY 2024

Abstract Convective Quasi-Equilibrium (CQE) is often adopted as a useful closure assumption to summarize the effects of unresolved convection on large-scale thermodynamics, while existing efforts to observationally validate CQE largely rely on specific spatial domains or sites rather than the source of CQE constraints—deep convection. This study employs a Lagrangian framework to investigate leading temperature perturbation patterns near deep convection, of which the centers are located by use of an ensemble of satellite measurements. Temperature perturbations near deep convection with high peak precipitation are rapidly adjusted toward the CQE structure within the [−2, 1] hours centered on peak precipitation. The top 1% precipitating deep convection constrains neighboring free-tropospheric leading perturbations up to 9°. Notable CQE validity beyond a 1° radius is observed when peak precipitation exceeds the 93rd percentile. These findings suggest that only a small fraction of deep convection with extreme precipitation shapes tropical free-tropospheric temperature patterns dominantly.

Plain Language Summary Convective Quasi-Equilibrium (CQE) is a concept in atmospheric science that explains a state where the influence of deep convection (cumulonimbus clouds) and large-scale atmospheric forces is balanced, causing certain thermodynamic properties to adjust toward specific reference profiles. Previous studies have focused on how temperature changes relate to the CQE structure but in specific regions or sites while this study aims areas near deep convection—supposedly the source of CQE constraints. Using a unique framework with data from multiple satellites, we track the evolution of temperature patterns near deep convection and find temperatures near deep convection with extreme rainfall are adjusted toward the CQE structure rapidly within 3 hr of maximum rainfall. However, only the deep convection with top 7% extreme rainfall can effectively affect nearby temperature pattern beyond 1°, with the top 1% influencing up to an 9° radius. These findings highlight the dominant impact of a small fraction of deep convection, particularly those with extreme rainfall, on nearby temperature perturbation patterns.

1. Introduction

The Convective Quasi-Equilibrium (CQE) theory, first introduced by Arakawa and Schubert (1974), posits that convective energy within cumulus ensemble remains in statistical equilibrium, balanced between large-scale replenishment and cloud-scale consumption. Intrinsic to the equilibrium, moist convection actively steers vertical temperature perturbations toward specific reference profiles, a principle embedded in various moist convective adjustments (Ahmed et al., 2020; Betts, 1973; Betts & Miller, 1986; Kuo, 1974; Manabe et al., 1965) and parameterizations (Chikira & Sugiyama, 2010; Frierson, 2007; Moorthi & Suarez, 1992; Randall & Pan, 1993; T. Wu, 2012; G. J. Zhang & McFarlane, 1995; Zhao et al., 2018). Such adjustment of vertical temperature structures is facilitated by analytic solutions (Emanuel et al., 1994; Yu & Neelin, 1997) to develop tropical intermediate complexity models (Neelin & Zeng, 2000; Sobel & Neelin, 2006; Zeng et al., 2000) and has shown to have a profound effect within deep convective areas by observations (Holloway & Neelin, 2007; Li et al., 2022; W. Wu et al., 2006; Xu & Emanuel, 1989).

Deep convection, often characterized by its robust updraft core and expansive cirrus anvil canopy, has predominantly been studied using satellite observations to discern its thermodynamic characteristics across temporal and spatial scales (Del Genio & Kovari, 2002; Feng et al., 2011; Houze et al., 2015). Collocating polar-orbiting and geostationary satellites enables the monitoring of three-dimensional thermodynamic structures within deep

convection (Chakraborty et al., 2016; Chung et al., 2008; Takahashi & Luo, 2014), where the Mesoscale Convective System (MCS) plays a crucial role — contributing over half of tropical precipitation (Feng et al., 2021; Nesbitt et al., 2006; Roca et al., 2014; Schumacher & Rasmussen, 2020; Yuan & Houze, 2010). The presence of a convective core and its characteristics, including depth, width, intensity, and shape, influences the behavior of MCSs (D. Wang et al., 2020; Zheng et al., 2018). Algorithms utilizing geostationary satellites have been employed to track the convective core and its associated MCS generating comprehensive global data sets for research communities (Feng et al., 2021; Fiolleau & Roca, 2013; Huang et al., 2018).

Despite extensive validations showing the proximity of tropical temperature perturbation profiles to those constrained by the CQE theory, the spatial domains were confined to specific sites or regions across observations, that is, a Eulerian framework (Holloway & Neelin, 2007; Li et al., 2022; Nie et al., 2010) and models (Lin et al., 2015; X. Wang et al., 2022). This leaves an intriguing gap unexplored: the immediate vicinity of tropical deep convection, presumably to be the primary force shaping temperature structures. This gap prompts us to ask: Do temperature perturbations near tropical deep convection follow Convective Quasi Equilibrium? If so, when, where, and to what extent do they exhibit this behavior? Addressing these questions is crucial for advancing our understanding of the fundamental mechanisms driving convective processes and their influence on the broader atmospheric dynamics. To bridge this gap, a Lagrangian framework integrating an MCS-tracking database and CloudSat retrieval to pinpoint the center of deep convective systems is used to quantitatively assess when the temperature perturbations, within a certain radius relative to the center, adhere to the CQE structure.

2. Data and Methodology

2.1. Data

The CloudSat satellite is equipped with a 94 GHz Cloud Profiling Radar (CPR) that detects cloud and precipitation particles. The CPR has a high-resolution footprint of approximately 1.7 km along track and 1.3 km across track with a vertical resolution of 480 m. Its active sensing capabilities enable the radar data to provide detailed vertical cloud structures. The Tracking Of Organized Convection Algorithm through a 3-D Segmentation (TOOCAN) is a specialized tool developed for detecting and tracking MCS using infrared imagery from geostationary satellites (Fiolleau & Roca, 2013). The clustering method within TOOCAN utilizes an iterative process across horizontal and temporal dimensions to decompose brightness temperature regions under 235 K into several MCSs by repeating growing regions starting at 190 K with a 5-K increment. To identify deep convection, radar reflectivity and cloud mask data from the CloudSat satellite's 2B-GEOPROF product (Marchand et al., 2008), and morphological parameters of MCS mass center locations (latitude, longitude, time) along the life cycles from the TOOCAN database, are employed.

In this study, we examine the hourly temperature field using the European Center for Medium-Range Weather Forecasts' fifth global reanalysis (ERA-5; Hersbach et al., 2020). In addition to temperature data across all available pressure levels, we also extract total precipitation data from the ERA5 to identify the peak precipitation, which further aligns the analyzed time series with hour 0 indicating the peak precipitation and conditions on strong convection events. Both TOOCAN and ERA-5 data are harmonized to a temporospatial resolution of $0.25° \times 0.25°$ and hourly increments to ensure their congruence.

Within the scope of this study, only MCS objects with track of the mass center confined within 30° north and south in latitude over lands and oceans are examined. To align with the data availability across the CloudSat, TOOCAN, and ERA-5, we analyze data only for the year 2013. Note that only the ascending (daytime) observations of CloudSat at around local time 13:30 is used here due to its battery anomaly since 2011.

2.2. Locating Centers of Deep Convection

In this manuscript, we focus on well-developed MCSs that contain at least one deep convective core (DCC), detected by CloudSat, within its coverage at any given time during its lifespan recognized by TOOCAN. The DCC criteria encompass continuous radar echo from cloud top to within 2 km of the surface, an echo of at least 10 dBZ above 10 km, and an attaching anvil horizontally spanning over 20 km with its base above 5 km, similar to previous works (Takahashi & Luo, 2012; Takahashi et al., 2017, 2021, 2023). This integration of continuous monitoring from geostationary satellites and vertical-penetration ability from polar-orbiting satellite prevents misclassification based solely on cold brightness temperature (Liu et al., 2007) and facilitates accurate tracking of

deep convection centers. Note that the TOOCAN data over the western South Pacific is not available because the routine scanning schedule of the MTSAT-2 satellite, being operated during the study period, did not allow as frequent observations as optimal for cloud tracking in the southern hemisphere. Although the centers are found using integrating satellite products, subsequent Lagrangian analysis exclusively relies on ERA-5 reanalysis data due to its capacity to capture temporal evolution across a vast three-dimensional domain equally inside and outside clouds unlike infrared satellite sounding.

2.3. Characterizing Temperature Perturbations Near Deep Convection

All following calculations and illustrations in this section are conducted within a specified radius from the convection centers. The radius is chosen from 1 to 10° (or roughly from 100 to 1,000 km) to study the horizontal-scale dependence. For each convection object, defined as an MCS recognized by TOOCAN with an embedded DCC detected by CloudSat, we identify the peak precipitation hour at every grid throughout its life duration and extract the hourly temperature profiles within 24 hr before and after accordingly. The temperature perturbations are obtained by subtracting a mean temperature profile averaged over the relative [−24,24] hours within the radius. To investigate temperature behaviors influenced by convection intensity, a threshold for peak precipitation exceeding a specific percentile, ranging from the 80th to 99th percentile, is calculated and applied across the radial distance, relative hours, and convection objects. For each hour, the temperature perturbations conditioned on the peak precipitation over the 368 observed deep convective objects at each level are regressed against those in the free troposphere, defined between 850 and 200 hPa, resulting in a single regression coefficient. The vertical profile of regression coefficients, same as that presented in Holloway and Neelin (2007), depicts the leading hourly pattern of temperature perturbations observed within the radius, reflective of a specific convection intensity.

2.4. Quantifying Similarity of Temperature Perturbations to the Theoretical CQE Structure

The theoretical temperature perturbation profile constrained by CQE, to be compared with the leading observational profile, is referred to as the A-profile afterward for simplicity. The A-profile is a function of temperature profile under assumptions of hydrostatic approximation, ideal gas law, and Clausius–Clapeyron relation (see detailed derivations in Li et al., 2022, modified from Yu & Neelin, 1997):

$$A(p,T(p)) \equiv \frac{T'(p)}{T'(p_0)} = \left(\frac{p_{LCL}}{p_0}\right)^{\kappa} \frac{1+\gamma(T(p_{LCL}))}{1+\gamma(T(p))} \exp\left(-\kappa \int_{p}^{p_{LCL}} \frac{1}{1+\gamma\left(T\left(p'\right)\right)} d\ln p'\right), p > p_{LCL}, \quad (1)$$

and

$$A(p,T(p)) \equiv \left(\frac{p}{p_0}\right)^{\kappa}, p > p_{LCL}, \quad (2)$$

where p is pressure, T temperature, T' the temperature perturbation from climatology, p_0 the reference level, p_{LCL} the lifting condensation level, $\gamma \equiv \frac{\varepsilon e_s l_v^2}{c_{pd} p R_v T^2}$ with $\varepsilon \equiv \frac{R_d}{R_v} = 0.622$ the ratio of gas constant for dry air R_d to that for water vapor R_v, e_s the saturation vapor pressure with respect to liquid, $l_v = 2.5 \times 10^6$ J/kg the latent heat of vapourization, $c_{pd} = 1004$ J/kg/K the specific heat of dry air at constant pressure, and $\kappa \equiv \frac{R_d}{c_{pd}}$.

For simplicity, the individual A-profile is calculated with $p_0 = 1{,}000$ hPa and $p_{LCL} = 950$ hPa by input of temperature profile interpolated to a 5-hPa interval at each grid and hour, without considering entrainment. To compare with the regression coefficient profiles, the A-profile is averaged within the [−24, 24] hours and within the given radius, then normalized to have unity root mean square over the free troposphere. Unless specifically noted, the term A-profile refers to the normalized A-profile hereafter. These settings are considered practical given the robust statistics of A-profiles in the tropics and the nature of A-profile illustrating proportions between vertical levels (Li et al., 2022). Finally, to quantify similarity between the A-profile and regression coefficient profile, vertical spatial correlation and root-mean-square deviation (RMSD) are calculated over the free troposphere.

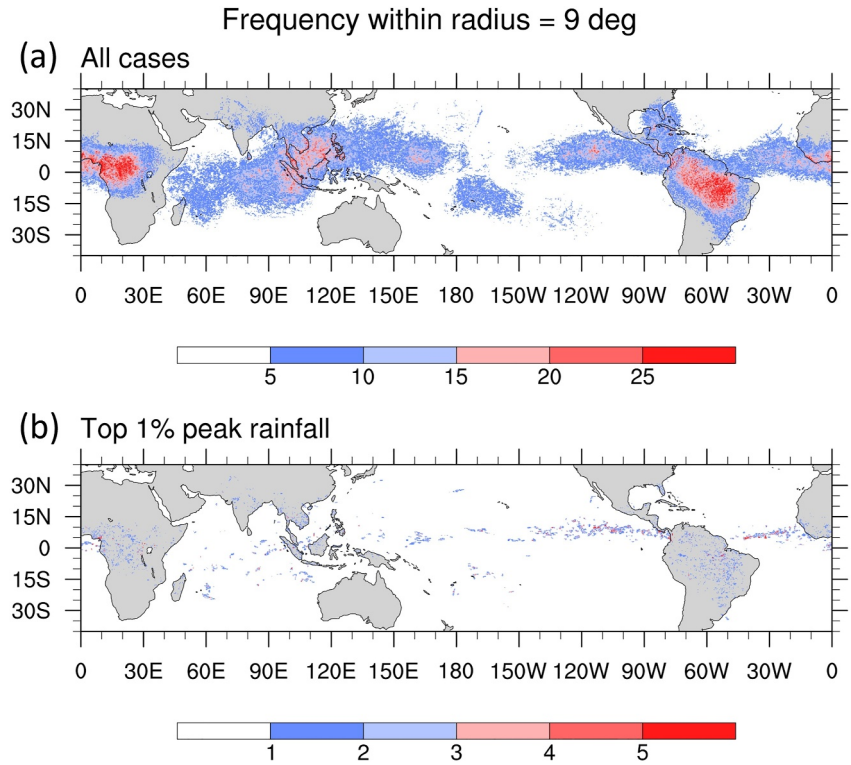

Figure 1. Number of extracted temperature profiles at each 0.25° grid within 9 degrees of tropical deep convection centers for (a) all instances regardless of peak precipitation and (b) instances where the peak precipitation surpasses the 99th percentile (c.f., method) in the year of 2013.

3. Results and Discussions

3.1. Spatial Distribution of Temperature Perturbations Extracted Near Deep Convection

Prior to comparing the A-profile and regression coefficient profile for their similarity, we explore the geographical distribution of collocated deep convection distribution to comprehend where the temperature perturbations are analyzed.

Figure 1a shows the count of extracted temperature profiles spanning [−24, 24] hours near tropical deep convection within a specific radius of 9° from the deep convection centers, irrespective of precipitation intensity. The 9° radius is selected because it represents the maximum distance where the CQE constraint on temperature appears valid, as later detailed in Section 3.3. The pattern generally corresponds to the ITCZ climatology, with more deep convection over the continents, especially the Amazon and west Africa, compared to the oceans. To further examine the temperature structure in conjunction with extreme precipitation, Figure 1b manifests the number of extracted samples over grids where peak precipitation exceeds the 99th percentile of all instances. Similarly, it captures a greater prevalence of extreme convective columns over continents than over oceans. The sensitivity tests with different radii demonstrate no significant changes on the geographic patterns in both cases (not shown), where the land-sea contrast of deep convection occurrences has been observed by previous studies (Liu & Zipser, 2005; Liu et al., 2007; Takahashi & Luo, 2014; Takahashi et al., 2017; Wang et al., 2019).

Note that Figure 1b does not mark where mass centers of deep convection or intense DCCs locate but directly pinpoints the grids collocated with intense precipitation within the specified 9° radius. Compared to an examination at the MCS scale, which analyzes every grid within the radius of top 1%-precipitating MCSs (not shown), this analysis at the individual grid level notably reduces noise among temperature perturbations. Such a difference likely arises due to inhomogeneous precipitation pattern within MCSs and the spatial discrepancy between the satellite-identified mass center and the ERA-5 precipitation center. The missing data over the Southwest Pacific in the TOOCAN data set (see Section 2.2), roughly between 115°E−175°E, may appear concerning because of frequent identification of DCCs (Takahashi & Luo, 2014; Takahashi et al., 2017). However, this region

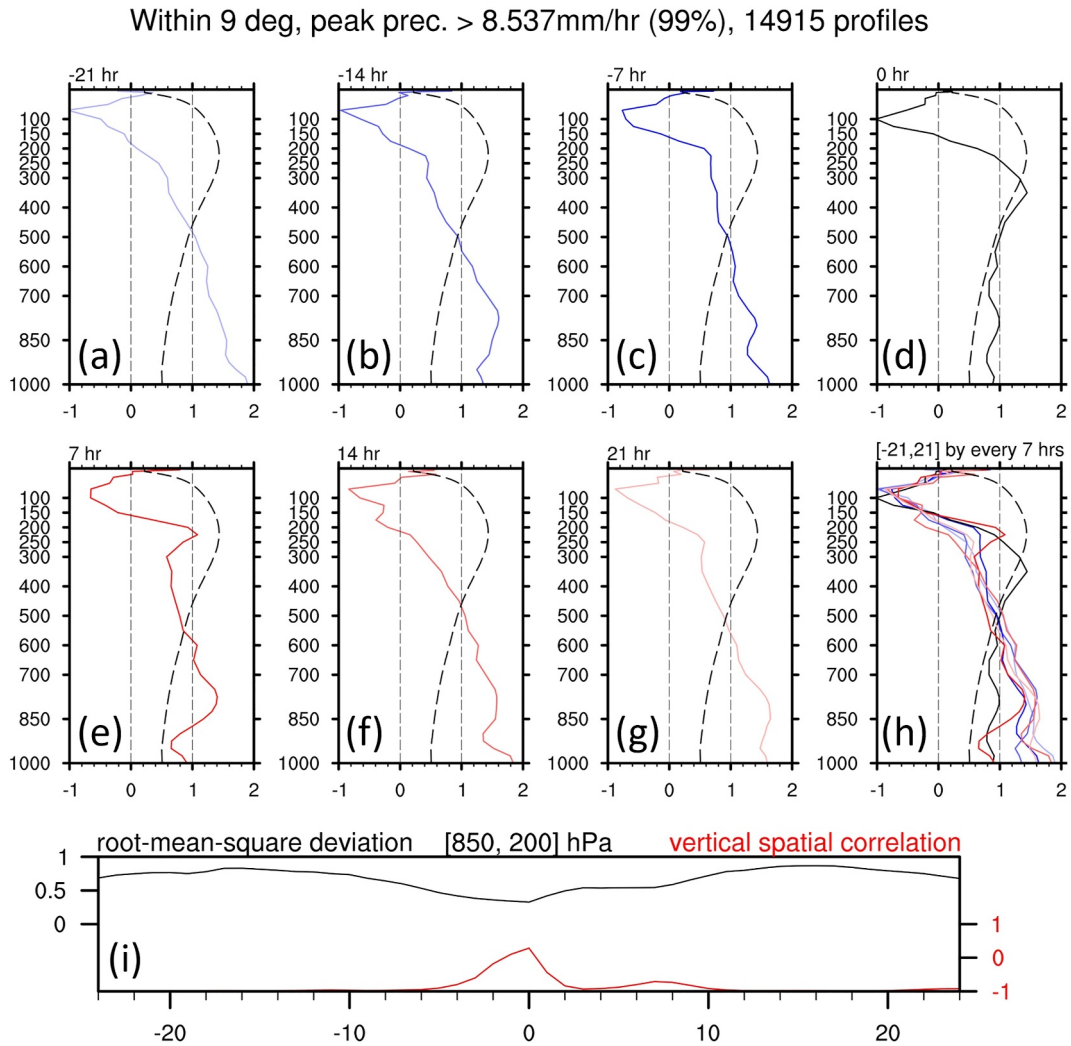

Figure 2. (a) The A-profile (dashed) and vertical profile of regression coefficients (colored) of the temperature perturbations within an 9° radius conditioned on the peak precipitation exceeding the 99th percentile at each level against the vertically averaged free troposphere. The regression coefficient profile is calculated at −21 hr relative to the peak precipitation hour. (b)–(g) As in panel (a), but for −14, −7, 0, 7, 14, and 21 hr, respectively. Note that lighter colors indicate hours farther away from the 0 hr. (h) Collection of all the profiles shown in panels (a)–(g) for comparison. (i) The hourly time series of root-mean-square deviation (black) and vertical spatial correlation (red) between the A-profile and the regression coefficient profile over the troposphere.

contributes relatively less to the global occurrence of tropical deep convection observed with coexisting high radar echo top height and low cloud top brightness temperature (Liu et al., 2007). Therefore, while the absence of data poses a constraint, its impact on the study's outcomes and conclusions could be regarded as minor.

3.2. Leading Observations and Their Similarity to the CQE Theoretical Structure

To derive the representative profile of observational temperature perturbations for comparison with the A-profile, or the CQE theoretical structure, we adopt the regression method from Holloway and Neelin (2007). The regression coefficients represent the slope of the regression and can be interpreted as expected temperature change at the given level with a 1-K change in the vertically averaged free tropospheric temperature. Figures 2a–2g display the A-profile (dashed line) and leading observational patterns (colored lines) obtained through the regression at specific hours relative to the peak precipitation with a 7-hr interval, and Figure 2h collects all these profiles for a comprehensive comparison. Note that the profiles are calculated using temperature profiles conditioned on the 99th percentile peak precipitation (8.537 mm/hr) within an 9° radius of the deep convection

centers, corresponding to the 14,915 occurrences distributed in Figure 1b. To quantify the similarity between the regression coefficient profile and A-profile, Figure 2i showcases the time series of RMSD and vertical spatial correlation, both computed over the free troposphere between 850 and 200 hPa at each hour. Of special note is that the vertical spatial correlation is identical to the cosine similarity between profiles, and hence a positive correlation suggests a leading temperature perturbation profile that increases with height, mirroring the A-profile pattern within the free troposphere. All correlations mentioned in the text refer to the vertical spatial correlation.

Throughout most hours, the leading temperature perturbations tend to decrease with altitude in the free troposphere, opposing that seen in the A-profile, as depicted in Figures 2a–2c and 2e–2g. The prevailing shallow cumulus with substantial entrainment might be a cause of the bottom-heavy structure (Lin et al., 2015; Singh & O'Gorman, 2013), which leads to negative correlations and elevated RMSD in Figure 2i. This suggests that at an hourly scale or within a day, the CQE principle is mostly limited (Donner & Phillips, 2003; Lin et al., 2015; G. J. Zhang, 2003). In contrast, the highest correlation and lowest RMSD occur at the peak hour, flanked by abrupt increases within the [−4, 2] hour range. The correlations at the [−2, 1] hours are found significantly different from all hours beyond the [−2, 1] hour window with a 95% confidence level using Fisher's Z-test. This is consistent with Figure 2d, which captures similar increasing perturbations with height between both profiles over the free troposphere, remarkably closely aligned between 700 and 300 hPa. The convective cold top, marked by a negative minimal perturbation around 100 hPa (Holloway & Neelin, 2007), remains consistently robust across all the hours. All the observational characteristics mentioned above hold true when assessed across different radii and peak-precipitation thresholds within the [89th, 99th] percentile range except for the higher correlations found for tighter radii and stricter thresholds (not shown). The rest of the manuscript will exclusively utilize the correlation to assess the CQE validity on temperature, as RMSD exhibits a similar response with opposite trend.

3.3. CQE Validity as a Function of Relative Hour, Relative Distance and Peak Precipitation Percentile

We have demonstrated how top-1%-precipitating temperature perturbations align with the A-profile near deep convection, focusing on evolution of the vertical leading patterns. To provide a more comprehensive scrutiny, we validate the proximity of temperature perturbations to the CQE structure using spatial vertical correlation as a function of the hour relative to peak precipitation, distance relative to the deep convection centers, and the threshold percentile of the peak precipitation.

Figure 3a suggests that the CQE robustly constrains the leading temperature perturbations within the [−2, 1] hour. For each radius, Fisher's Z-test at a 95% confidence level is performed at each hour to identify significantly different hours by comparing the correlation at each hour with those at all the hours 3 hours before and after. The positive correlation reaches the farthest distance of 9° during the peak hour with significant differences observed within [2, 9] degrees, along with the maximum correlation of ∼0.86 among all hours. The robustness of the CQE constraints on temperature within the 3 hr aligns with the timescale of convective adjustment commonly considered (see Section 5b in a review of Arakawa, 2004). This supports the CQE principle that convective adjustment is relatively fast compared to large-scale forcing. Interestingly, the influence of the CQE on temperature appears more profound one hour before the peak precipitation, where the positive correlation reaches 9° with significant differences within [3, 10] degrees, compared to one hour after, where it reaches 7° with significant difference limited within [4, 8] degrees. In addition, the correlations at the −2 hr are significantly positive within [−3,7] degrees while those at the 2 hr are all negative without significance. Such asymmetric horizontal extent of validity can be observed by conditioning on percentiles equal to or higher than 95% (not shown). The CQE constraints on temperature quickly deteriorate after 1 hour following the peak precipitation, causing temperature perturbations to deviate from the CQE more rapidly than the build-up of positive correlations before the peak hour. This aligns with the observations that the peak of the first baroclinic mode, or deep convective mode favoring the CQE structure, is followed by the peak of second baroclinic mode, which on the contrary disfavors the CQE (Masunaga & L'Ecuyer, 2014). Note that, while the second baroclinic mode could act against CQE, the smoothing effect of horizontal temperature perturbations is still efficient by means of fast dry gravity waves.

Notably, other positive correlations appear around [−22, −15] and [12, 17] hours, primarily confined within a 1° radius. The hourly time series of maximum precipitation among the top 1% precipitating grids suggests that this phenomenon is likely due to a few extreme precipitation events which happen to peak around these hours (not shown) while these minor peak correlations are more pronounced when considering a smaller radius and higher

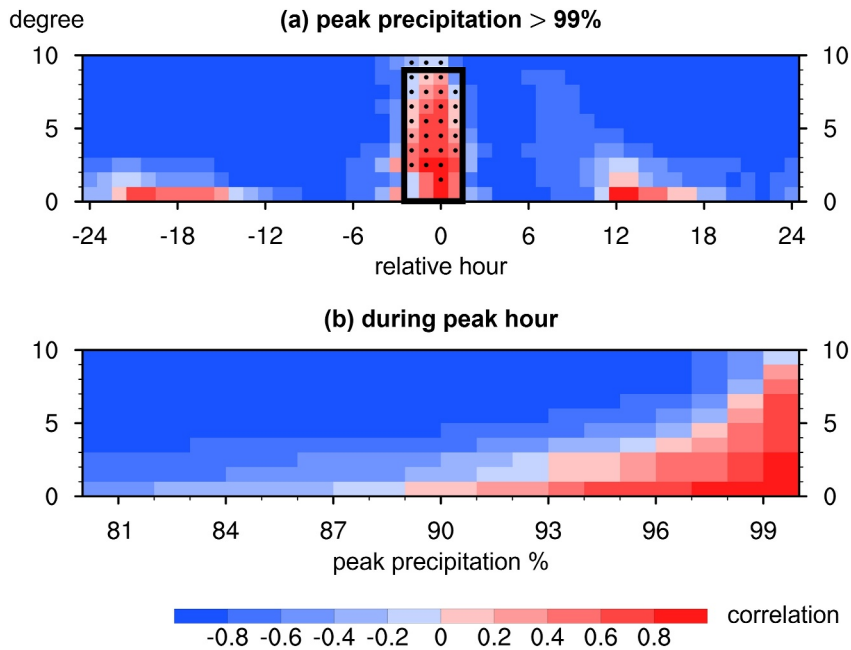

Figure 3. (a) Vertical spatial correlation between the regression coefficient profiles using temperature perturbations conditioned on peak precipitation exceeding the 99th percentile and the A-profile over the free troposphere. Each box indicates the correlation at a specific hour relative to the peak precipitation (*x*-axis, spanning from −24 to 24 hr in 1 hr increments) within a certain radius with respect to the deep convection center (*y*-axis, extending from 1 to 10° in 1° increments). The black box indicates the [−2, 1] hours interval and the black dots represent the hours that are significantly different. (b) As in panel (a), but the correlations are calculated at the peak hour using temperature perturbations exceeding different percentile thresholds of the peak precipitation (*x*-axis, ranging from 80% to 99% in 1% increments).

peak precipitation (not shown). Note that these secondary peaks are not statistically significant (i.e., not hatched in Figure 3a).

Figure 3b demonstrates that during the hour of peak precipitation, only the leading temperature perturbations with the top 10% peak precipitation exhibit a comparable pattern of increasing perturbations with height, akin to the CQE structure within a 1° radius, while only those in the top 7% extend beyond 1°. This suggests that not all convective objects can effectively adjust the neighboring temperature through the CQE constraints, but only the extreme ones among deep convection. This is consistent with the "circus tent" concept, which suggests that deep convection with the highest free-tropospheric saturation moist static energy (or the sub-cloud moist static energy, theoretically equivalent as expected from the CQE), play a dominant role in convective adjustment processes in the tropics (Bao et al., 2021; Williams et al., 2023; Zhou & Xie, 2019). The high threshold of peak precipitations and the minor peaks of positive correlations in Figure 3 both reinforce our understanding that most of the CQE constraints arise from a very small fraction of deep convection, consistent with previous literature (Bao & Stevens, 2021).

4. Concluding Remarks

Although previous studies have extensively examined the validity of CQE on temperature, many of them have focused on specific spatial domains or sites, that is, a Eulerian framework, rather than directly addressing the source of CQE constraints—deep convection. This study aims to investigate the evolution of leading temperature perturbation patterns near deep convection, consisting of MCSs identified by stationary satellites and deep convective cores observed by the CloudSat at a time. By employing a Lagrangian framework following the deep convection centers, this approach enables the quantification of when, where, and to what extent these perturbations resemble the CQE structure. Our key findings for the broad tropics (30°N–30°S) can be succinctly summarized as follows:

- (When) Conditioned on the top 1% peak precipitation and within the relative [−2, 1] hours,
- (Where) temperature perturbations obeying the CQE structure, defined as a positive vertical spatial correlation between the free-tropospheric leading observational and analytic theoretical profiles, reaches a distance up to 9°,
- (To what extent) accompanied by higher correlations before the peak precipitation than after, with a maximum correlation of ∼0.86 during the peak hour.

These results suggest that temperature perturbations near deep convection are rapidly adjusted toward the CQE structure in a few hours, consistent with the idea that the weak temperature gradient approximation allows tropical gravity waves to rapidly propagate strong signals from deep convection to affect the surrounding environmental temperature (Ahmed et al., 2021; Bretherton & Smolarkiewicz, 1989; Sobel et al., 2001; Y. Zhang & Fueglistaler, 2020). Within such a short timeframe, on the order of an hour, the CQE's influence on temperature is noticeable only when analyzing grids where peak precipitation exceeds the 89th percentile, implying that only a small fraction of deep convection is capable of influencing the neighboring temperature over distances greater than 100 km. Temperature perturbations with the top 1% peak precipitation near deep convection conform to the CQE structure up to 9° from the centers during the peak hour, as one might expect from the typical Rossby radius of deformation, which ranges from hundreds to thousands of kilometers.

Most importantly, this study underscores the dominant role of deep convection with extreme precipitation in shaping the leading patterns of tropical free-tropospheric temperature. Our approach reflects the composite temporospatial pattern of deep convective clusters under different precipitation intensities. The findings suggest that the observed invalidity of CQE in a fine temporal resolution in previous studies, where non-deep-convective, ordinary-deep-convective, and extreme-deep-convective events are not carefully separated from each other, leading to a deviated macrostate from an equilibrium dominated by extreme deep convection. On the other hand, the current method in this paper actively focuses on the prime impacts of intense deep convection that are deliberately chosen for analysis. It is important to note that these two perspectives do not conflict; the traditional view tends to be a passive observation over a mixed environment with occasional random deep convection. Since deep convection occurs frequently and randomly across the tropics, our approach bridges the gap between the role of individual convective systems and their collective consequences on the tropical regions.

It is important to note that the conclusion largely depends on the selection of domain. When narrowing down from the broad tropics (30N–30S) to equatorial (10N–10S) band, the vertical pattern of regression coefficients does not alter much across the [−24, 24] hours and degrees of radii, and resembles that of Figure 2d with high correlation with the A-profile (see Figure S1a). The pattern with high correlation exhibits for any threshold of peak precipitation percentile larger than zero while for a direct comparison, Figure S1c maintains the same abscissa values used in Figure 3b. As the deep tropics is more favorable for deep convection, the temperature perturbations tend to be closer to the A-profile in the upper troposphere. Such high CQE validity may be also associated with the high frequency of extreme precipitation events, which tends to occur within the deep tropics (c.f., Figure 1b). With the help of weak temperature gradient effect, deep tropical grids are frequently and continuously covered by the large impact radius of extreme convections, shaping the tropospheric temperature close to the A-profile at any hour (see Figure S1b). For the deep tropics (10°N–10°S), the conclusion of "when, where, and to what extent" changes to

- (When) peak precipitation is non-zero, the peak-hour temperature perturbations
- (Where) obeying the CQE structure is ubiquitous,
- (To what extent) accompanied by positive vertical spatial correlations throughout the [−24, 24] hours.

However, to discuss and yield conclusions applicable for a broad tropical region, the manuscript focuses on the findings using the domain of 30° north and south as Section 2.1 states.

The current study provides an interesting angle in understanding how valid the CQE constrains tropical free-tropospheric temperature near the deep convection in a Lagrangian view. However, owing to the requirement of monitoring vertical temperature structure changes with a high spatiotemporal resolution, the ERA-5 reanalysis data is utilized here instead of comparable satellite observations as those used during the collocation of deep convection. Also, although the collocation strengthens our confidence of collecting well-developed MCSs coincided with deep convective cores at a certain time point, one cannot assure that deep clouds always exist around the mass centers along the evolution. Overall, we consider the methodological framework to be highly optimized for such an analysis but future work on improving the collocating procedures and expanding the

studying period, even toward how the CQE validity might change under a climate-change scale, is needed to further understand the relationship between the CQE and deep convection.

Data Availability Statement

Information about the CloudSat can be accessed through the CloudSat Data Processing Center, including the level-2 radar data used here (Marchand et al., 2008). Details regarding the Tracking Of Organized Convection Algorithm using a 3-dimensional segmentation are available (TOOCAN, 2019). The hourly temperature and precipitation data from ERA-5 are publicly accessible (Hersbach et al., 2020).

Acknowledgments
YXL was supported by the National Science and Technology Council in Taiwan through Grants 111-2111-M-008-062 and 112-2917-I-564-008. JYY was supported through Grants NSTC112-2811-M008-026. We express our gratitude to Dr. Thomas Fiolleau for his valuable discussions regarding the TOOCAN database and for granting public access to it.

References

Ahmed, F., Adames, Á. F., & Neelin, J. D. (2020). Deep convective adjustment of temperature and moisture. *Journal of the Atmospheric Sciences*, *77*(6), 2163–2186. https://doi.org/10.1175/JAS-D-19-0227.1

Ahmed, F., Neelin, J. D., & Adames, Á. F. (2021). Quasi-equilibrium and weak temperature gradient balances in an equatorial Beta-Plane Model. *Journal of the Atmospheric Sciences*, *78*(1), 209–227. https://doi.org/10.1175/JAS-D-20-0184.1

Arakawa, A. (2004). The cumulus parameterization problem: Past, present, and future. *Journal of Climate*, *17*(13), 2493–2525. https://doi.org/10.1175/1520-0442(2004)017<2493:ratcpp>2.0.co;2

Arakawa, A., & Schubert, W. H. (1974). Interaction of a cumulus cloud ensemble with the large-scale environment, Part I. *Journal of the Atmospheric Sciences*, *31*(3), 674–701. https://doi.org/10.1175/1520-0469(1974)031<0674:IOACCE>2.0.CO;2

Bao, J., & Stevens, B. (2021). The elements of the thermodynamic structure of the tropical atmosphere. *Journal of the Meteorological Society of Japan. Ser. II*, *99*(6), 1483–1499. https://doi.org/10.2151/jmsj.2021-072

Bao, J., Stevens, B., Kluft, L., & Jimenez-de-la-Cuesta, D. (2021). Changes in the tropical lapse rate due to entrainment and their impact on climate sensitivity. *Geophysical Research Letters*, *48*(18), e2021GL094969. https://doi.org/10.1029/2021GL094969

Betts, A. K. (1973). Non-precipitating cumulus convection and its parameterization. *Quarterly Journal of the Royal Meteorological Society*, *99*(419), 178–196. https://doi.org/10.1002/qj.49709941915

Betts, A. K., & Miller, M. J. (1986). A new convective adjustment scheme. Part II: Single column tests using GATE wave, BOMEX, ATEX and arctic air-mass data sets. *Quarterly Journal of the Royal Meteorological Society*, *112*(473), 693–709. https://doi.org/10.1002/qj.49711247308

Bretherton, C. S., & Smolarkiewicz, P. K. (1989). Gravity waves, compensating subsidence and detrainment around cumulus clouds. *Journal of the Atmospheric Sciences*, *46*(6), 740–759. https://doi.org/10.1175/1520-0469(1989)046<0740:GWCSAD>2.0.CO;2

Chakraborty, S., Fu, R., Massie, S. T., & Stephens, G. (2016). Relative influence of meteorological conditions and aerosols on the lifetime of mesoscale convective systems. *Proceedings of the National Academy of Sciences of the United States of America*, *113*(27), 7426–7431. https://doi.org/10.1073/pnas.1601935113

Chikira, M., & Sugiyama, M. (2010). A cumulus parameterization with state-dependent entrainment rate. Part I: Description and sensitivity to temperature and humidity profiles. *Journal of the Atmospheric Sciences*, *67*(7), 2171–2193. https://doi.org/10.1175/2010JAS3316.1

Chung, E.-S., Sohn, B.-J., & Schmetz, J. (2008). CloudSat shedding new light on high-reaching tropical deep convection observed with Meteosat. *Geophysical Research Letters*, *35*(2). https://doi.org/10.1029/2007GL032516

Del Genio, A. D., & Kovari, W. (2002). Climatic properties of tropical precipitating convection under varying environmental conditions. *Journal of Climate*, *15*(18), 2597–2615. https://doi.org/10.1175/1520-0442(2002)015<2597:CPOTPC>2.0.CO;2

Donner, L. J., & Phillips, V. T. (2003). Boundary layer control on convective available potential energy: Implications for cumulus parameterization. *Journal of Geophysical Research*, *108*(D22), 4701. https://doi.org/10.1029/2003JD003773

Emanuel, K. A., David Neelin, J., & Bretherton, C. S. (1994). On large-scale circulations in convecting atmospheres. *Quarterly Journal of the Royal Meteorological Society*, *120*(519), 1111–1143. https://doi.org/10.1002/qj.49712051902

Feng, Z., Dong, X., Xi, B., Schumacher, C., Minnis, P., & Khaiyer, M. (2011). Top-of-atmosphere radiation budget of convective core/stratiform rain and anvil clouds from deep convective systems. *Journal of Geophysical Research*, *116*(D23). https://doi.org/10.1029/2011JD016451

Feng, Z., Leung, L. R., Liu, N., Wang, J., Houze Jr, R. A., Li, J., et al. (2021). A global high-resolution mesoscale convective system database using satellite-derived cloud tops, surface precipitation, and tracking. *Journal of Geophysical Research: Atmospheres*, *126*(8), e2020JD034202. https://doi.org/10.1029/2020JD034202

Fiolleau, T., & Roca, R. (2013). An algorithm for the detection and tracking of tropical mesoscale convective systems using infrared images from geostationary satellite. *IEEE Transactions on Geoscience and Remote Sensing*, *51*(7), 4302–4315. https://doi.org/10.1109/TGRS.2012.2227762

Frierson, D. M. W. (2007). The dynamics of idealized convection schemes and their effect on the zonally averaged tropical circulation. *Journal of the Atmospheric Sciences*, *64*(6), 1959–1976. https://doi.org/10.1175/JAS3935.1

Hersbach, H., Bell, B., Berrisford, P., Hirahara, S., Horányi, A., Muñoz-Sabater, J., et al. (2020). The ERA5 global reanalysis [Dataset]. *Quarterly Journal of the Royal Meteorological Society*, *146*(730), 1999–2049. https://doi.org/10.1002/qj.3803

Holloway, C. E., & Neelin, J. D. (2007). The convective cold top and quasi equilibrium. *Journal of the Atmospheric Sciences*, *64*(5), 1467–1487. https://doi.org/10.1175/JAS3907.1

Houze, R. A. J., Rasmussen, K. L., Zuluaga, M. D., & Brodzik, S. R. (2015). The variable nature of convection in the tropics and subtropics: A legacy of 16 years of the Tropical Rainfall Measuring Mission satellite. *Reviews of Geophysics*, *53*(3), 994–1021. https://doi.org/10.1002/2015RG000488

Huang, X., Hu, C., Huang, X., Chu, Y., Tseng, Y.-h., Zhang, G. J., & Lin, Y. (2018). A long-term tropical mesoscale convective systems dataset based on a novel objective automatic tracking algorithm. *Climate Dynamics*, *51*(7), 3145–3159. https://doi.org/10.1007/s00382-018-4071-0

Kuo, H. L. (1974). Further studies of the parameterization of the influence of cumulus convection on large-scale flow. *Journal of the Atmospheric Sciences*, *31*(5), 1232–1240. https://doi.org/10.1175/1520-0469(1974)031<1232:FSOTPO>2.0.CO;2

Li, Y.-X., Neelin, J. D., Kuo, Y.-H., Hsu, H.-H., & Yu, J.-Y. (2022). How close are leading tropical tropospheric temperature perturbations to those under convective quasi equilibrium? *Journal of the Atmospheric Sciences*, *79*(9), 2307–2321. https://doi.org/10.1175/JAS-D-21-0315.1

Lin, J.-L., Qian, T., Shinoda, T., & Li, S. (2015). Is the tropical atmosphere in convective quasi-equilibrium? *Journal of Climate*, *28*(11), 4357–4372. https://doi.org/10.1175/JCLI-D-14-00681.1

Liu, C., & Zipser, E. J. (2005). Global distribution of convection penetrating the tropical tropopause. *Journal of Geophysical Research*, *110*(D23), D23104. https://doi.org/10.1029/2005jd006063
Liu, C., Zipser, E. J., & Nesbitt, S. W. (2007). Global distribution of tropical deep convection: Different perspectives from TRMM infrared and radar data. *Journal of Climate*, *20*(3), 489–503. https://doi.org/10.1175/JCLI4023.1
Manabe, S., Smagorinsky, J., & Strickler, R. F. (1965). Simulated climatology of a general circulation model with a hydrologic cycle. *Monthly Weather Review*, *93*(12), 769–798. https://doi.org/10.1175/1520-0493(1965)093<0769:SCOAGC>2.3.CO;2
Marchand, R., Mace, G. G., Ackerman, T., & Stephens, G. (2008). Hydrometeor detection using cloudsat—An Earth-orbiting 94-GHz cloud radar [Dataset]. *Journal of Atmospheric and Oceanic Technology*, *25*(4), 519–533. https://doi.org/10.1175/2007JTECHA1006.1
Masunaga, H., & L'Ecuyer, T. S. (2014). A mechanism of tropical convection inferred from observed variability in the moist static energy budget. *Journal of the Atmospheric Sciences*, *71*(10), 3747–3766. https://doi.org/10.1175/JAS-D-14-0015.1
Moorthi, S., & Suarez, M. J. (1992). Relaxed Arakawa-Schubert. A parameterization of moist convection for general circulation models. *Monthly Weather Review*, *120*(6), 978–1002. https://doi.org/10.1175/1520-0493(1992)120<0978:RASAPO>2.0.CO;2
Neelin, J. D., & Zeng, N. (2000). A quasi-equilibrium tropical circulation model—Formulation. *Journal of the Atmospheric Sciences*, *57*(11), 1741–1766. https://doi.org/10.1175/1520-0469(2000)057<1741:AQETCM>2.0.CO;2
Nesbitt, S. W., Cifelli, R., & Rutledge, S. A. (2006). Storm morphology and rainfall characteristics of TRMM precipitation features. *Monthly Weather Review*, *134*(10), 2702–2721. https://doi.org/10.1175/MWR3200.1
Nie, J., Boos, W. R., & Kuang, Z. (2010). Observational evaluation of a convective quasi-equilibrium view of monsoons. *Journal of Climate*, *23*(16), 4416–4428. https://doi.org/10.1175/2010JCLI3505.1
Randall, D. A., & Pan, D.-M. (1993). Implementation of the Arakawa-Schubert cumulus parameterization with a prognostic closure. In K. A. Emanuel & D. J. Raymond (Eds.), *The representation of cumulus convection in numerical models* (pp. 137–144). American Meteorological Society. https://doi.org/10.1007/978-1-935704-13-3_11
Roca, R., Aublanc, J., Chambon, P., Fiolleau, T., & Viltard, N. (2014). Robust observational quantification of the contribution of mesoscale convective systems to rainfall in the tropics. *Journal of Climate*, *27*(13), 4952–4958. https://doi.org/10.1175/JCLI-D-13-00628.1
Schumacher, R. S., & Rasmussen, K. L. (2020). The formation, character and changing nature of mesoscale convective systems. *Nature Reviews Earth & Environment*, *1*(6), 300–314. https://doi.org/10.1038/s43017-020-0057-7
Singh, M. S., & O'Gorman, P. A. (2013). Influence of entrainment on the thermal stratification in simulations of radiative-convective equilibrium. *Geophysical Research Letters*, *40*(16), 4398–4403. https://doi.org/10.1002/grl.50796
Sobel, A. H., & Neelin, J. D. (2006). The boundary layer contribution to intertropical convergence zones in the quasi-equilibrium tropical circulation model framework. *Theoretical and Computational Fluid Dynamics*, *20*(5), 323–350. https://doi.org/10.1007/s00162-006-0033-y
Sobel, A. H., Nilsson, J., & Polvani, L. M. (2001). The weak temperature gradient approximation and balanced tropical moisture waves. *Journal of the Atmospheric Sciences*, *58*(23), 3650–3665. https://doi.org/10.1175/1520-0469(2001)058<3650:TWTGAA>2.0.CO;2
Takahashi, H., & Luo, Z. (2012). Where is the level of neutral buoyancy for deep convection? *Geophysical Research Letters*, *39*(15). https://doi.org/10.1029/2012GL052638
Takahashi, H., & Luo, Z. J. (2014). Characterizing tropical overshooting deep convection from joint analysis of CloudSat and geostationary satellite observations. *Journal of Geophysical Research: Atmospheres*, *119*(1), 112–121. https://doi.org/10.1002/2013JD020972
Takahashi, H., Luo, Z. J., & Stephens, G. (2021). Revisiting the entrainment relationship of convective plumes: A perspective from global observations. *Geophysical Research Letters*, *48*(6), e2020GL092349. https://doi.org/10.1029/2020GL092349
Takahashi, H., Luo, Z. J., Stephens, G., & Mulholland, J. P. (2023). Revisiting the land-ocean contrasts in deep convective cloud intensity using global satellite observations. *Geophysical Research Letters*, *50*(5), e2022GL102089. https://doi.org/10.1029/2022GL102089
Takahashi, H., Luo, Z. J., & Stephens, G. L. (2017). Level of neutral buoyancy, deep convective outflow, and convective core: New perspectives based on 5 years of CloudSat data. *Journal of Geophysical Research: Atmospheres*, *122*(5), 2958–2969. https://doi.org/10.1002/2016JD025969
TOOCAN. (2019). Tracking Of Organized Convection Algorithm using a 3-dimensional segmentation version 2.06 [Dataset]. https://doi.org/10.14768/20191112001.1
Wang, D., Giangrande, S. E., Feng, Z., Hardin, J. C., & Prein, A. F. (2020). Updraft and downdraft core size and intensity as revealed by radar wind profilers: MCS observations and idealized model comparisons. *Journal of Geophysical Research: Atmospheres*, *125*(11), e2019JD031774. https://doi.org/10.1029/2019JD031774
Wang, J., Houze, R. A., Jr., Fan, J., Brodzik, S. R., Feng, Z., & Hardin, J. C. (2019). The detection of mesoscale convective systems by the GPM Ku-band spaceborne radar. *Journal of the Meteorological Society of Japan*, *97*(6), 1059–1073. Special Edition on Global Precipitation Measurement (GPM): 5th Anniversary. https://doi.org/10.2151/jmsj.2019-058
Wang, X., Zhang, G. J., & Suhas, E. (2022). Assessing free tropospheric quasi-equilibrium for different GCM resolutions using a cloud-resolving model simulation of tropical convection. *Climate Dynamics*, *59*(9), 3035–3050. https://doi.org/10.1007/s00382-022-06232-1
Williams, A. I. L., Jeevanjee, N., & Bloch-Johnson, J. (2023). Circus tents, convective thresholds, and the non-linear climate response to tropical SSTs. *Geophysical Research Letters*, *50*(6), e2022GL101499. https://doi.org/10.1029/2022GL101499
Wu, T. (2012). A mass-flux cumulus parameterization scheme for large-scale models: Description and test with observations. *Climate Dynamics*, *38*(3), 725–744. https://doi.org/10.1007/s00382-011-0995-3
Wu, W., Dessler, A. E., & North, G. R. (2006). Analysis of the correlations between atmospheric boundary-layer and free-tropospheric temperatures in the tropics. *Geophysical Research Letters*, *33*(20). https://doi.org/10.1029/2006GL026708
Xu, K.-M., & Emanuel, K. A. (1989). Is the tropical atmosphere conditionally unstable? *Monthly Weather Review*, *117*(7), 1471–1479. https://doi.org/10.1175/1520-0493(1989)117<1471:ITTACU>2.0.CO;2
Yu, J.-Y., & Neelin, J. D. (1997). Analytic approximations for moist convectively adjusted regions. *Journal of the Atmospheric Sciences*, *54*(8), 1054–1063. https://doi.org/10.1175/1520-0469(1997)054<1054:AAFMCA>2.0.CO;2
Yuan, J., & Houze, R. A. (2010). Global variability of mesoscale convective system anvil structure from A-train satellite data. *Journal of Climate*, *23*(21), 5864–5888. https://doi.org/10.1175/2010JCLI3671.1
Zeng, N., Neelin, J. D., & Chou, C. (2000). A quasi-equilibrium tropical circulation model—Implementation and simulation. *Journal of the Atmospheric Sciences*, *57*(11), 1767–1796. https://doi.org/10.1175/1520-0469(2000)057<1767:AQETCM>2.0.CO;2
Zhang, G. J. (2003). Convective quasi-equilibrium in the tropical Western Pacific: Comparison with midlatitude continental environment. *Journal of Geophysical Research*, *108*(D19), 4592. https://doi.org/10.1029/2003jd003520
Zhang, G. J., & McFarlane, N. A. (1995). Sensitivity of climate simulations to the parameterization of cumulus convection in the Canadian climate centre general circulation model. *Atmosphere-Ocean*, *33*(3), 407–446. https://doi.org/10.1080/07055900.1995.9649539

Zhang, Y., & Fueglistaler, S. (2020). How tropical convection couples high moist static energy over land and ocean. *Geophysical Research Letters*, *47*(2), e2019GL086387. https://doi.org/10.1029/2019GL086387

Zhao, M., Golaz, J.-C., Held, I. M., Guo, H., Balaji, V., Benson, R., et al. (2018). The GFDL global atmosphere and land model AM4.0/LM4.0: 2. Model description, sensitivity studies, and tuning strategies. *Journal of Advances in Modeling Earth Systems*, *10*(3), 735–769. https://doi.org/10.1002/2017MS001209

Zheng, J., Liu, D., Wang, Z., & Wang, Y. (2018). Differences among three types of tropical deep convective clusters observed from A-Train satellites. *Journal of Quantitative Spectroscopy and Radiative Transfer*, *217*, 253–261. https://doi.org/10.1016/j.jqsrt.2018.05.006

Zhou, W., & Xie, S.-P. (2019). A conceptual spectral plume model for understanding tropical temperature profile and convective updraft velocities. *Journal of the Atmospheric Sciences*, *76*(9), 2801–2814. https://doi.org/10.1175/jas-d-18-0330.1